Available online at www.sciencedirect.com

ScienceDirect

Acta Materialia 79 (2014) 292–303

Acta MATERIALIA

www.elsevier.com/locate/actamat

In situ quantification of the nucleation and growth of Fe-rich intermetallics during Al alloy solidification

C. Puncreobutr [a,b], A.B. Phillion [c], J.L. Fife [d], P. Rockett [a], A.P. Horsfield [b], P.D. Lee [a,*]

[a] School of Materials, The University of Manchester, Oxford Road, Manchester, UK
[b] Department of Materials, Imperial College London, Prince Consort Road, London, UK
[c] School of Engineering, The University of British Columbia, Kelowna, Canada
[d] Swiss Light Source, Paul Scherrer Institut, 5232 Villigen PSI, Switzerland

Received 19 January 2014; received in revised form 10 July 2014; accepted 10 July 2014
Available online 16 August 2014

Abstract

Real-time in situ synchrotron X-ray tomographic microscopy was used to gain new insights into and quantify the nucleation mechanisms and growth kinetics of β-Al_5FeSi intermetallics during solidification of an aluminium Al–7.5Si–3.5Cu–0.6Fe (wt.%) alloy. Three new insights were obtained. First, the plate-like β-intermetallics appeared to nucleate mainly on or near the primary aluminium dendrites and to a lesser extent off the oxide skin on the surface of the specimen. Second, for this alloy composition, β-intermetallic formation was largely complete before the formation of Al–Si eutectic. Third, the β-intermetallics formed via fast lateral growth, wrapping around and in between the primary dendrite arms. Further, the nucleation and growth dynamics of β-intermetallics were quantified as a function of undercooling in a functional form that could be easily used in microstructural simulations. The frequency of intermetallic interaction mechanisms, such as plate nucleation vs. impingement and branching, were also quantified.

Keywords: Intermetallics; Aluminium–silicon–copper alloys; In situ solidification; Synchrotron X-ray tomographic microscopy

1. Introduction

The size and morphology of secondary phases in many alloys are key to the resulting properties of the material, ranging from the strengthening effect of γ'-precipitates via dislocation pinning in Ni-base superalloys [1] to grain refinement in steels [2]. However, secondary phases can also be harmful; for example, they can initiate fatigue failure [3], as well as accelerate solidification defect growth and propagation [4–6].

In Al–Si alloys, secondary phase formation provides one of the most widely used strengthening mechanisms, through age hardening, but it also limits the use of material recycling in many engineering applications, especially when fatigue life is critical [3]. A major impurity element in Al-alloys that influences detrimental secondary phase formation is Fe, which is frequently acquired at levels of 0.4–0.8 wt.% from Al scrap during the recycling process [7,8]. During solidification, such large Fe levels may lead to the formation of highly faceted plate-like β-Al_5FeSi intermetallics. These plate-like intermetallics, which appear as needles in 2-D optical micrographs, are hard and brittle, and have low cohesion with the aluminium matrix [9]. Therefore, they can degrade mechanical properties, such as elongation and fatigue, of cast components [10]. They have also been reported to contribute to the formation of solidification defects, such as porosity [4,5,11–13] and hot tearing [4,14].

Prior experimental studies on the control of Fe intermetallics in Al alloys have ranged from studying the influence of alloying elements (e.g. Mn, Sr, V and TiB_2) on

* Corresponding author.
E-mail addresses: peter.lee@manchester.ac.uk, p.d.lee@ic.ac.uk (P.D. Lee).

http://dx.doi.org/10.1016/j.actamat.2014.07.018
1359-6454/

intermetallic morphology [15–17] to the application of rapid solidification to minimise the size of the intermetallic [18]. Although there have been a wide variety of experiments, understanding of the nucleation mechanisms and growth kinetics of the β-intermetallics remains limited. This knowledge is needed to control the nucleation process and to improve casting quality.

Recent experimental studies have focused on the use of in situ methodologies to reveal the complexity of β-intermetallic nucleation and growth [7,19,20]. In Wang et al., fast in situ X-ray radiography (acquired at 2 Hz) identified an initial lateral growth spurt after nucleation of the β-intermetallics, followed by a slow thickening during the later stages of solidification [7]. Kim et al. also observed similar growth behaviour of β-intermetallics in Al alloys with varying Fe contents using radiography [19]. A previous in situ 3-D synchrotron X-ray tomography experiment confirmed both the initial rapid growth in the lateral direction and the slow thickening rate of the intermetallics [20]. In Ref. [20], 3-D scans were captured every 57 s at a cooling rate of 1.4 °C min^{-1}, which provided insufficient information to resolve the initial nucleation and growth stages of the intermetallics.

In the present study, in situ 3-D X-ray tomographic microscopy was performed on a solidifying Al–7.5Si–3.5Cu–0.6Fe (wt.%) specimen incorporating two acquisition speeds: one to capture the full solidification sequence and a second, higher speed to quantify the nucleation and growth of the β-Al_5FeSi intermetallics. Quantification of these 4-D images (three spatial dimensions evolving in time) provides new insights into the complex evolution of intermetallics and their interactions with the primary phase.

2. Methods

An aluminium A319 alloy with a nominal composition of Al–7.5Si–3.5Cu–0.6Fe (wt.%, measured as Al–7.52Si–3.53Cu–0.59Fe–0.07Mg–0.07Ti–<0.01Mn) was prepared using a commercial Al-A319 ingot (courtesy of Ford Motor Company, USA) and a commercially pure Al–10 wt.% Fe master alloy (courtesy of London and Scandinavian Metallurgical Co. Ltd., UK). To prepare this alloy, the metals were first melted at 730 °C in a clay-bonded graphite crucible within an electric resistance furnace, then cast into a preheated permanent mould [21] to form a wedge-shaped specimen. Cylindrical specimens 2.5 mm in diameter and 4 mm in length were machined along the isotherm direction using wire electric discharge machining in preparation for the in situ solidification studies. The as-cast secondary dendrite arm spacing (λ_2) was approximately 30 μm. Prior studies have shown that many forms of Fe-rich intermetallics can exist in the A319 alloy system [15,22,23]. One study by Wang et al. [13] on this specific alloy composition and similar solidification conditions concluded from energy-dispersive X-ray spectroscopy that the plate-like intermetallics were most likely the β-Al_5FeSi intermetallic phase. Therefore, the term β-Al_5FeSi is used in this paper for all plate-like Fe-rich intermetallics.

The in situ solidification experiments were performed at the TOMCAT beamline of the Swiss Light Source (Paul Scherrer Institut, Switzerland) [24,25] using a bespoke resistance furnace with six enclosed alumina heaters. The furnace was designed with a central hole allowing insertion and rotation of the specimen, with sidewall X-ray-transparent windows to allow the X-ray beam to pass through. The specimens were contained in high-purity boron nitride (BN) holders that were fitted on top of a pyrophyllite rod attached to the rotation stage, as shown in the schematic in Fig. 1a, with the entire setup shown in Fig. 1b. The inner diameter of the BN holder was slightly larger than the specimen's diameter to allow for stress-free thermal expansion during heating. A K-type thermocouple was placed underneath the specimen holder to measure the temperature during the experiments.

The experimental procedure consisted of first gradually heating the specimen to 650 °C, isothermally holding for 5 min to ensure the specimen completely melted, then cooling at a controlled rate of 3 °C min^{-1} until the specimen was fully solidified. During solidification, fast X-ray tomographic microscopy was conducted [26], collecting 1001 projections over 180° of rotation every 2 s. Polychromatic radiation was filtered to 5% power, which provided an average peak energy of approximately 30 keV. The detector consisted of an optical microscope designed for polychromatic radiation and incorporated a continuously adjustable magnification tuned close to 4×. When coupled with a high-speed CMOS camera (PCO DIMAX, Germany), the resulting pixel size was 2.75 μm.

Fast tomographic imaging ensured that the microstructural evolution within each 3-D dataset was small because the temperature change in 2 s was ~0.1 °C; this minimised artefacts in the resulting reconstructions typically caused by interface motion (due to microstructure evolution) during the scan.

Two in situ experiments with identical solidification conditions were completed using different delay times between subsequent 3-D volume acquisitions. The time between acquisitions is referred to as downtime. In the first (slow speed) experiment the downtime was 70 s, and in the second (high speed) experiment it was 10 s. The total capture interval between scans, where the total time includes acquisition of one full 3-D volume and downtime before the next scan, was thus 72 and 12 s in the first and second experiments, respectively. In the first experiment, the downtime of 70 s was used to transfer the acquired data out of the camera memory and onto the file server, allowing an unlimited number of scans to be captured and thus the full solidification sequence to be recorded. In contrast, with the shorter downtime of 10 s, the tomographic datasets were stored in the camera memory and only transferred at the end of the experiment. Thus, 13 scans were captured before the camera memory was full (as determined by the size of our cropped field of view). While the short downtime

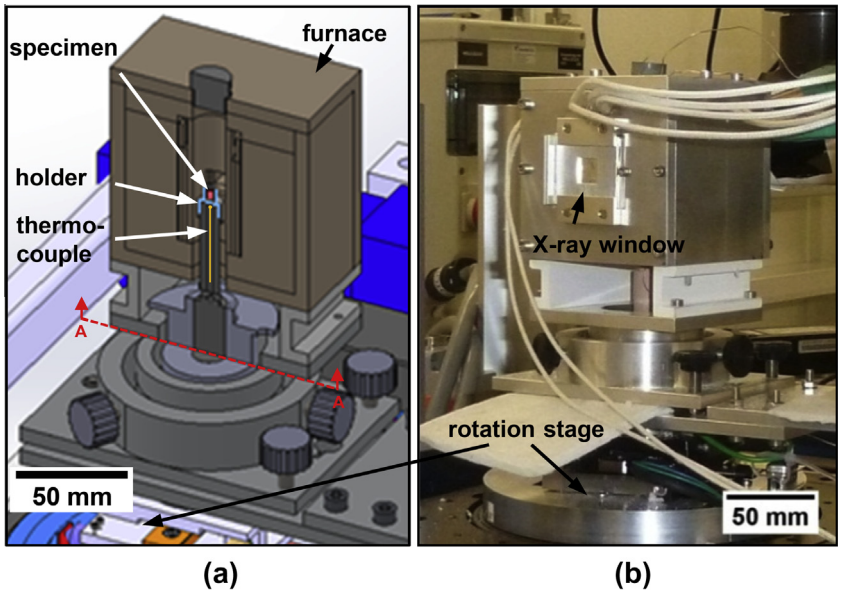

Fig. 1. (a) Cross-sectional schematic of the experimental setup and (b) photograph of the furnace mounted at the TOMCAT beamline of the SLS.

allowed for faster temporal resolution and thus quantification of the rapid initial growth of the β-intermetallic particles, the 13 datasets only recorded a small portion of the full solidification range, from 580 to 574 °C, hence the need for the first experiment. It should be noted that the beginning of the tomographic imaging in the second experiment was chosen based on observations in the first experiment; this ensured that the rapid initial growth stage of the β-intermetallics was captured.

The tomographic projections were reconstructed using algorithms based on Fourier transform methods [27,28]. From these 2-D slices, the 3-D volumes were generated and aligned using a 3-D affine registration method [29], followed by noise reduction using a 3-D anisotropic diffusion filter [30]. Image segmentation was then applied to distinguish the different phases of the microstructure. A 3-D region growing algorithm [31] was used to separate primary aluminium, aluminium–silicon eutectic (if present) and pores from the solidifying liquid, while manual segmentation was used to select the β-intermetallics. The segmented β-intermetallics were then individually separated and labelled based on connected regions and orientations. Finally, a particle tracking algorithm [32] was applied to track the growth of individual β-intermetallics in time.

Once the process of segmenting the various phases within a 3-D volume was complete, quantitative image analysis was performed on each volume. A combination of principal component analysis, marching cubes triangulation, skeletonisation and Euclidean distance transforms was used to quantify orientation and growth evolution (such as volume, length, growth rate and thickness) of each tracked β-intermetallic [33,34]. Quantitative image analysis was performed on sub-volumes ($400 \times 400 \times 400$ voxels ($\sim$1 mm^3)) in the first experiment, shown in Fig. 2b, reducing computational time whilst capturing a statistically significant number ($\sim$250) of intermetallics during the later stages of solidification when the β-intermetallic growth rate is slow. Quantitative image analysis was performed on the full volumes in the high-speed experiment to capture the early nucleation stages for a large number ($\sim$950) of intermetallics. The 3-D measurements were performed using Matlab (MathWorks, USA), while visualisation of the 3-D structures used Avizo (VSG, France).

3. Results and discussion

3.1. Solidification sequence

A series of images from the slow-speed 4-D X-ray tomographic microscopy experiment are shown in Fig. 2 to qualitatively illustrate the microstructural evolution during the solidification of the Al–7.5Si–3.5Cu–0.6Fe (wt.%) specimen. Segmented 3-D images of the various phases in the microstructure are shown in Fig. 2a, c, e, g and i, while longitudinal 2-D views are shown in Fig. 2b, d, f, h and j. The first occurrences of primary aluminium dendrites, shown in Fig. 2b, are seen at 600 °C. They appear slightly darker than the solidifying liquid due to the lower X-ray attenuation of the primary α-Al dendrites as compared to the Cu-enriched interdendritic liquid. As the growth and coarsening of α-Al proceeds, the attenuation contrast increases due to the continual partitioning of Cu to the liquid phase. Fig. 2c shows the partially solidified α-Al phase at 582 °C in three dimensions. At the next capture interval (72 s later, 578 °C, Fig. 2e), a few β-intermetallics have appeared and are rendered in three dimensions, and these are also visible as the white phase in Fig. 2f. The intermetallics appear white because they are more attenuating than either the α-Al or the liquid. The β-intermetallics continue to grow and new ones also nucleate as the temperature decreases further to 572 °C (Fig. 2g and h). Although not shown in Fig. 2, the formation of β-intermetallics was observed to

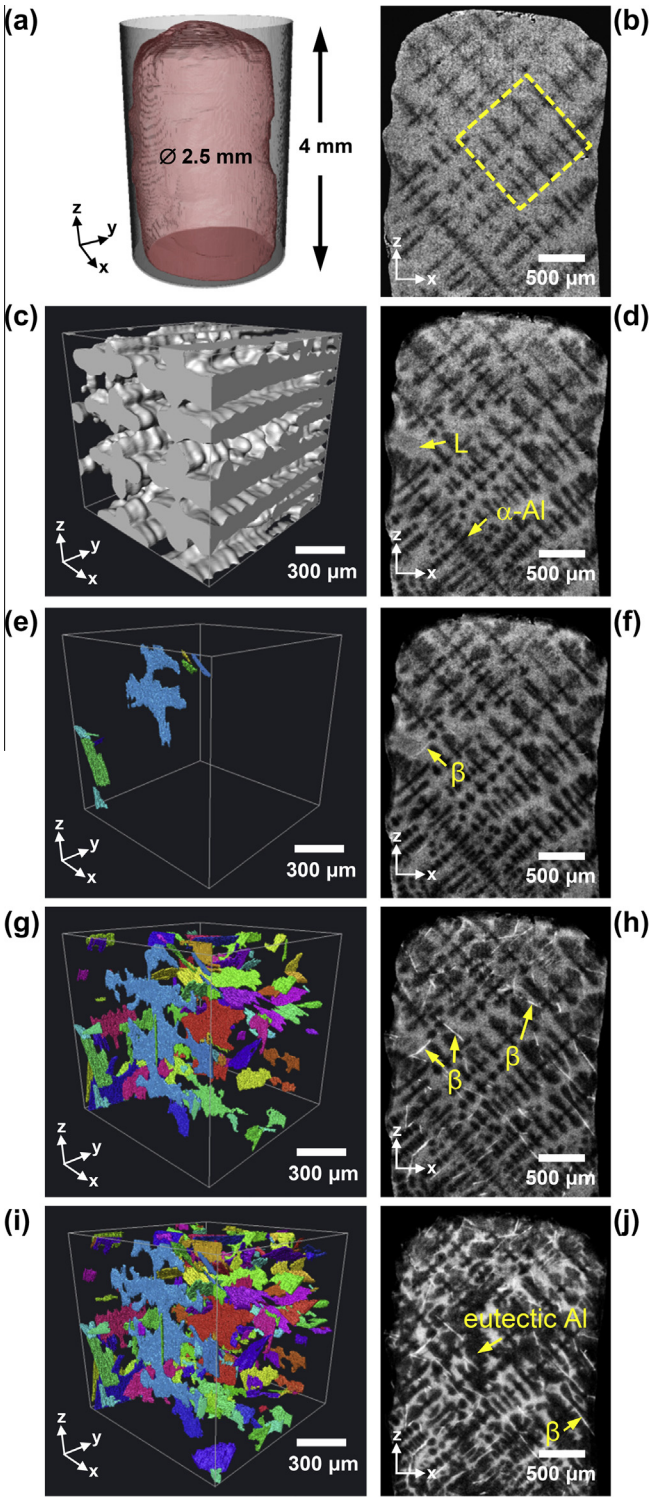

Fig. 2. (a) Rendering of the specimen (red) inside the BN holder, (b, d, f, h, j) typical 2-D longitudinal views of microstructure evolution during solidification of Al–7.5Si–3.5Cu–0.6Fe (wt.%), (c) 3-D rendering of the dendritic structure and (e, g, i) 3-D renderings of the β-intermetallics (different colours are used to separate the different intermetallics, whereas the same colour is kept for the same intermetallic at different temperatures). The microstructures and rendered volumes represent temperatures of (b) 600, (c, d) 582, (e, f) 578, (g, h) 572 and (i, j) 550 °C, respectively. Note that these results were taken from the first experiment, where the scan interval was 72 s. (For interpretation of the references to colour in this figure legend, the reader is referred to the web version of this article.)

be largely complete by 565 °C, while the formation of the Al–Si eutectic was first observed at 561 °C. The eutectic was observed to nucleate at or nearby the surface of the α-Al dendrites, as inferred previously from quenched [35] and in situ [36] solidification experiments. As it was not the goal of this study to resolve the Al–Si eutectic, for simplicity, it is considered as a single phase in the following analyses. The large number of β-intermetallics is shown in Fig. 2i and j (550 °C).

Only plate-like intermetallics were observed to form in this in situ solidification study. As outlined in the methods section and in Ref. [13], these intermetallics are most likely the β-Al_5FeSi intermetallic phase. It is possible that fine β-intermetallics and/or other Fe-based particles have formed but cannot be resolved in the tomographic images due to spatial resolution limitations.

While the entire solidification sequence is observed in the slow-speed experiment, more detailed observations of the nucleation and growth kinetics of β-intermetallics are captured by the high-speed experiment. Fig. 3 shows the evolution of intermetallic formation as captured by this high-speed experiment. Focusing on nucleation, the first visible β-intermetallic is at 579 ± 1 °C (Fig. 3a), which is in good agreement with the estimated temperature of nucleation from the slow-speed experiment (580 ± 2 °C, i.e. the average temperature between Fig. 2c and e). These values also agree well with previous experimental studies [7,20] and the Scheil predictions (580 °C) using CALPHAD (Thermo-Calc Software AB, Stockholm, with the database from Ref. [37]). In the subsequent images (Fig. 3b–f), these initial intermetallics grow while others nucleate and then grow as well. The nucleation events of both primary Al dendrites and intermetallics were first observed near the corners of the specimen. This is due to the presence of a slight thermal gradient across the specimen, since the surface is colder than the centre.

The evolution of volume fraction of β-intermetallics observed in both experiments is plotted in Fig. 4, along with the Scheil predictions using CALPHAD. Good agreement is found between the experimentally observed volume fraction of the β-intermetallics and the predicted value (2.1%). From the experimental solidification path, it can be seen that nearly 90% of the total volume of the β-intermetallic phase forms via a eutectic reaction of $L \rightarrow \alpha\text{-Al} + \beta\text{-}Al_5FeSi$ at temperatures well above the Al–Si eutectic. The formation of these two eutectic components appears to be weakly coupled, with the α-Al evolving through further growth of existing aluminium dendrites while the β-intermetallic appears to nucleate, in most cases, on and/or near the α-Al dendrites. Terzi et al. [20] previously observed irregular eutectic growth, suggesting that this eutectic reaction could occur either through coupled or uncoupled formation, but found it typically occurs close to a divorced eutectic. Our results suggest, instead, that the eutectic forms through a weakly coupled interaction. Although neither result is conclusive, both results confirm that strongly coupled eutectic formation is not present.

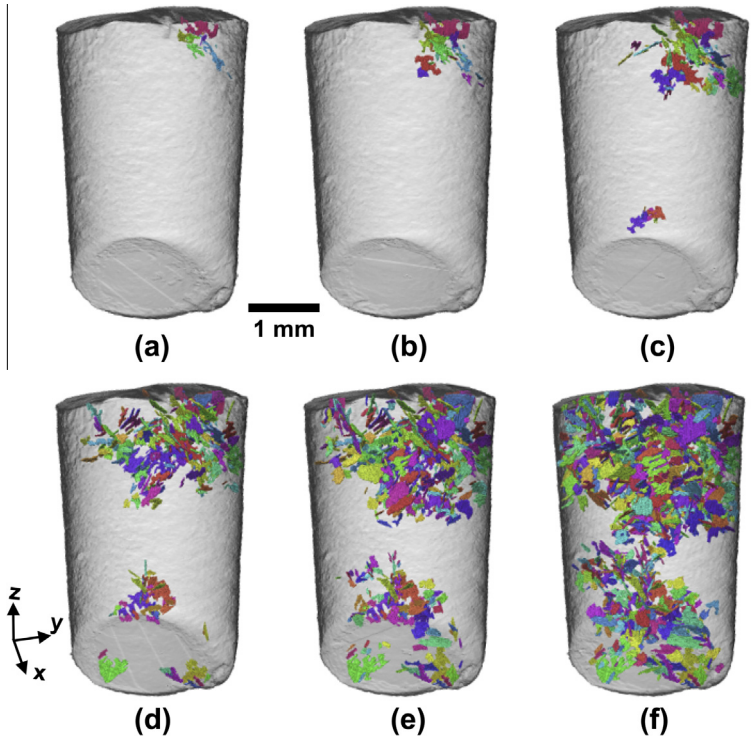

Fig. 3. Evolution of intermetallic formation at (a–f) 579, 578, 577, 576, 575 and 574 °C, respectively. Note that these results were taken from the second experiment, where the scan interval was 12 s.

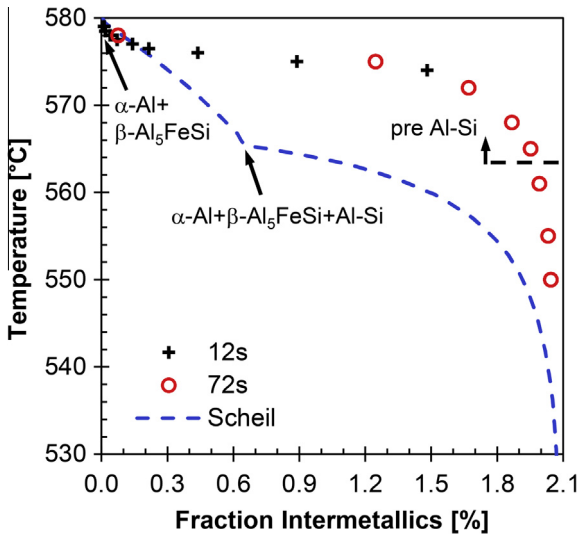

Fig. 4. Volume fraction of the β-intermetallic phase as quantified from both the first and second experiments and compared to calculations from the Scheil solidification model.

Below the eutectic temperature, development of an additional 10% volume fraction of β-intermetallics is observed (previously proposed in Ref. [15] to be via a ternary eutectic reaction of $L \rightarrow \alpha\text{-Al} + \text{Al–Si} + \beta\text{-Al}_5\text{FeSi}$). Similar results were reported in Refs. [7,13,15,20] over a range of cooling rates. Neither this observation nor the majority of β-intermetallic formation discussed above follow the thermodynamic prediction seen in Fig. 4, which predicts nearly 70% of the β-intermetallics preferentially form below the Al–Si eutectic temperature. This suggests that the Scheil model with the database from [37] may not be suitable for predicting the various stages of intermetallic growth.

3.2. Nucleation mechanisms

Fig. 5 shows a histogram of β-intermetallic nucleation density vs. nucleation temperature and nucleation undercooling. This result was determined via quantitative image analysis of both the slow and fast experiments using numerical tools previously developed to study pore nucleation [38]. A bin size of 1 °C was used, and the nucleation undercooling (ΔT_n) was estimated based on the difference between the observed nucleation temperature (T_n) and the thermodynamically predicted nucleation temperature (580 °C [37]). As Fig. 5 shows, β-intermetallics were observed to nucleate over a wide temperature range, between 579 and 568 °C, with a mode of 574 °C. The first β-intermetallic was observed at 579 °C. The nucleation start temperature of 579 °C corresponds to a solid fraction of ~0.3, which is greater than the dendrite coherency point for this alloy ($f_s \sim 0.21$), as measured in a prior equiaxed solidification study [39]. From the tomographic images, the structure consists of α-Al dendrites that are nearly touching.

A Gaussian distribution was then fitted to the histogram in Fig. 5 in order to characterise the nucleation density as a function of nucleation undercooling according to the classical equation [40]:

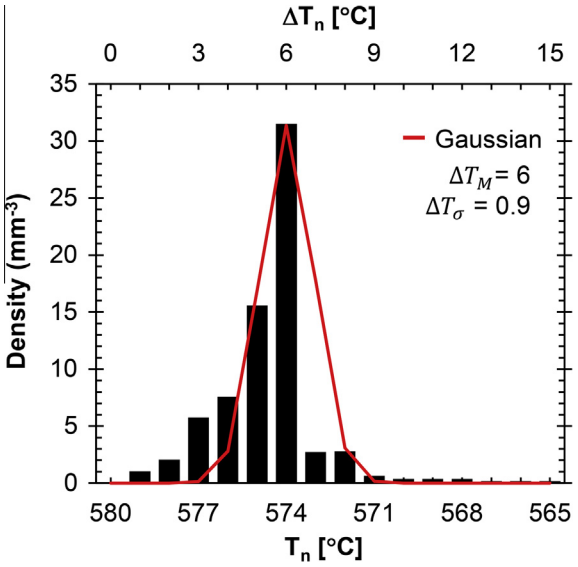

Fig. 5. Histogram of the nucleation density of the intermetallic phase as a function of nucleation temperature (T_n) and nucleation undercooling (ΔT_n). The Gaussian distribution fit of the histogram is also shown in red. (For interpretation of the references to colour in this figure legend, the reader is referred to the web version of this article.)

$$n = n_{max} \exp\left(-\frac{(\Delta T_n - \Delta T_M)^2}{2\Delta T_\sigma^2}\right) \quad (1)$$

where n is the nucleation density of β-intermetallics per unit volume, n_{max} is the maximum nucleation density, ΔT_n is the nucleation undercooling, and ΔT_M and ΔT_σ are the mean and deviation of the Gaussian nucleation undercooling distribution, respectively. In this study, where the casting was slow cooled at 3 °C min^{-1}, ΔT_M and ΔT_σ were found to be 6 and 0.9 °C, respectively, while the maximum activated nucleation density (n_{max}) was approximately 32 mm^{-3}. Eq. (1), together with these values, can be used in analytical or numerical microstructure models of solidification to extend predictions to include intermetallic nucleation, as previously demonstrated by Gandin and Rappaz [41] for grain growth and Lee and Hunt [38] for pore formation.

In addition to the nucleation temperature, the location of β-intermetallics nucleation can also be quantified. Prior studies suggested that nucleation was on the surface oxide [20,42]; however, the present results show that nucleation occurs throughout the volume of the specimen, both away from and near the specimen surface. Four main nucleation mechanisms were identified in the high-speed experiment and are highlighted in Fig. 6. The first three, captured in a small volume of ~0.1 mm^3 at the top right of the specimen shown in Fig. 3, are rendered in Fig. 6a–f, while another, similar volume was rendered in Fig. 6g and h. The four mechanisms are:

1. *Surface oxide nucleation:* the specimen surface, almost certainly Al_2O_3, was hypothesised to be an active nucleation site for β-intermetallics by Terzi et al. [20]. This study also observed nucleation on the surface. As shown in Fig. 6a and b, the red β-intermetallic first appears to be in contact with the specimen surface without contacting any of the surrounding pink β-intermetallics.

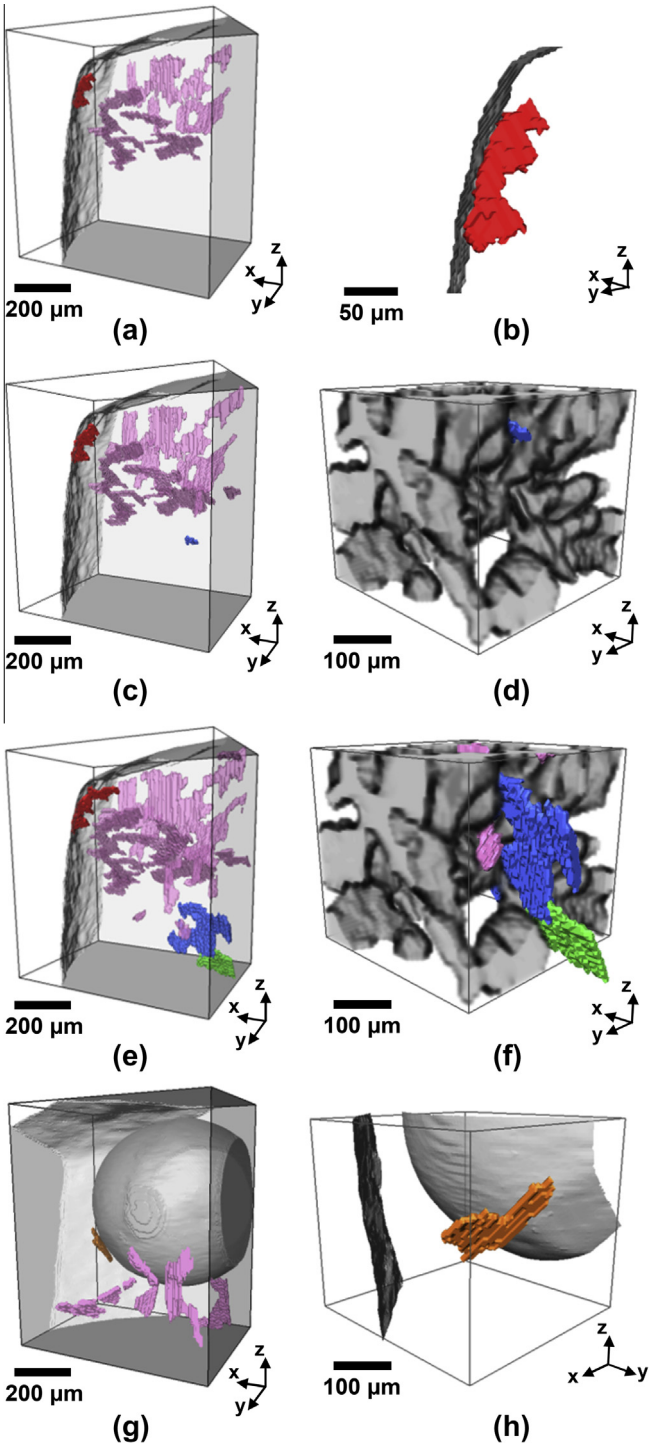

Fig. 6. Examples of β-intermetallic nucleation mechanisms: (red intermetallic in a and b) on the specimen surface, (blue intermetallic in c and d) on/near the α-Al dendrite, (green intermetallic in e and f) on an existing intermetallic and (orange intermetallic in g and h) on an as-cast porosity. Al-dendrites and pores are rendered in grey, whereas the surrounding intermetallics are rendered in pink. Rendered volumes represent temperatures of (a, b) 579, (c, d) 578.5, (e, f) 578 and (g, h) 576 °C, respectively. (For interpretation of the references to colour in this figure legend, the reader is referred to the web version of this article.)

2. *On/near α-Al dendrites:* nucleation also occurred in the bulk of the specimen, on or near the existing α-Al phase, as shown in blue in Fig. 6c and d.
3. *Self-nucleation:* intermetallics themselves also acted as nucleation sites for new β-intermetallics, as shown in Fig. 6e and f. At a distance from the specimen surface, the green β-intermetallic first appears to be in contact with the pre-existing blue β-intermetallic.
4. *Oxide skin of pores:* the oxide skin of pores also acted as a nucleation site for the β-intermetallic, as shown in Fig. 6g and h. The orange β-intermetallic forms on a pre-existing as-cast pore without connection to any surrounding pink β-intermetallics.

The high-speed tomographic images were thoroughly analysed in order to classify every β-intermetallic according to the above categories. This classification is summarised in Fig. 7, which reveals that each of the four types of nucleation sites were active over a wide range of temperatures. The results confirm the observations of previous studies [43,44], which suggested that alumina is an active nucleant for the β-intermetallic. However, unlike prior studies that suggested alumina on the surface was the prevailing nucleation mechanism (e.g. [20]), this work shows that nucleation at oxides was only one of many possible mechanisms. Further, quantification of all nucleation events demonstrated that the main mechanism of nucleation was on/near aluminium dendrites, occurring in 617 of 959 events, or ~64% of the time. The identification of the additional mechanisms is attributed to the faster acquisition times in this study, resolving the nucleation of β-intermetallics on/near dendrites and subsequent growth

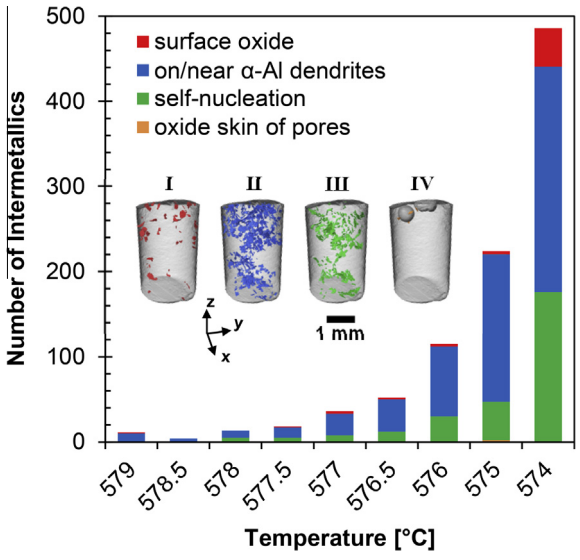

Fig. 7. Quantified β-intermetallic nucleation rates, as classified by the four types of nucleation sites. Insets I–IV illustrate intermetallics that were nucleated on the surface oxide, on/near the α-Al dendrites, on existing intermetallics (self-nucleation) and on the oxide skin of pores, respectively. Note that each intermetallic is rendered as it first appeared in the specimen.

out to the specimen surface. However, capturing a full 3-D image every 12 s did not always resolve nucleation vs. impingement. It should be noted that, although other, previously reported nucleation mechanisms for β-intermetallics were not observed in this study, including small entrained oxide films [43,45], double oxide films (bi-films) [46] and aluminium phosphide nucleant [15,47], their occurrence cannot be ruled out due to the spatial resolution limitations of this study.

To further explore the nucleation events on/near α-Al dendrites, the relationship between β-intermetallic nucleation orientation and aluminium dendrites was quantified. The normal vector of each β-intermetallic plate was determined using principle component analysis, producing a pole figure of the plate orientation relative to the secondary dendrite arm growth direction, as shown by the schematic inset in Fig. 8. A β-intermetallic is shown in red and its normal is shown with a corresponding arrow: if a β-intermetallic is perpendicular to the direction of the secondary dendrite arm(s), a dot is plotted at the centre of the figure; if the plate is parallel to the secondary dendrite arm(s), the dot is located on the circumference of the figure. By integrating all the dots, a contour plot is obtained, with higher concentrations shown in red. This is termed morphological texture in metals [48] or fabric in soils [49].

The morphological texture of the β-intermetallic plates that nucleate on/near the α-Al dendrites is shown in Fig. 8a, and the majority of the texture is located on the outer circumference of the contour plot. This indicates that the plates grow parallel to the secondary dendrite arms. Further, the normal vectors of these β-intermetallics fit a standard Gaussian distribution with $\mu = 88.8°$ and $\sigma = 43.5°$. This suggests that the majority of β-intermetallics that nucleated on/near the α-Al grow with a preferential orientation that matches the 4-fold crystallographic symmetry of the primary phase; this further indicates that they nucleated from the primary phase itself. Note that the intermetallics that did not nucleate on/near α-Al were relatively randomly oriented (see Fig. 8b), implicating the presence of other active nucleation sites such as oxides or foreign particles, as previously observed in Refs. [15,20,43,45].

3.3. Growth kinetics

After nucleation and during the initial growth stage, β-intermetallics evolve very rapidly in the lateral direction. Initially, the β-intermetallics grow within the interdendritic liquid with a thin, plate-like morphology (Fig. 9a), then the geometry becomes more complex with increasing size and impingement on the primary phase. To continue growing, the β-intermetallics wrap around the α-Al, creating complex shapes like branches and holes (Fig. 9b and c). The growth propagates through even narrow gaps between dendrite arms, spreading out into open regions past the constraint (e.g. the region indicated by the arrow in Fig. 9b). Thus, despite the presence of obstructing dendrite

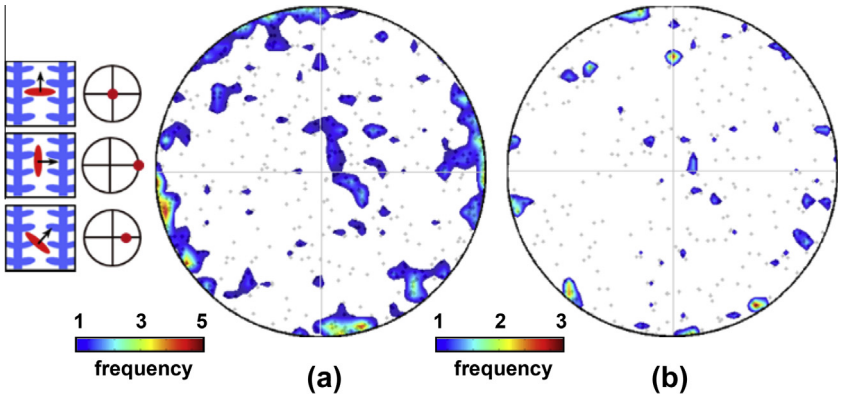

Fig. 8. Orientation contour plot of the normal distribution of (a) intermetallics nucleated on/near α-Al dendrites and (b) intermetallics nucleated elsewhere, as compared to the growth directions of the secondary dendrite arms. Each grey dot in (a) and (b) represents the normal of each plate. The insets illustrate how each grey dot was determined.

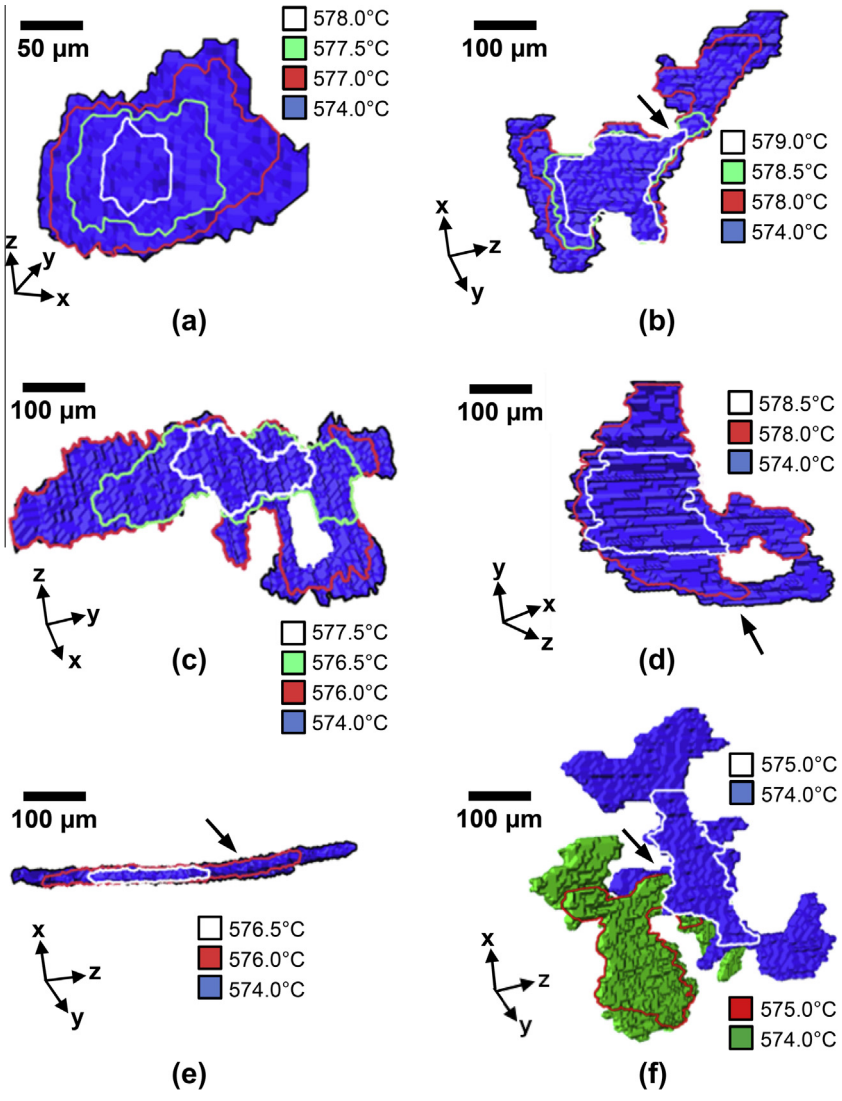

Fig. 9. The different growth evolutions of β-intermetallics during solidification: (a) standard plate-like growth, (b, c) growth of complex plate-like shapes, (d) growth around a dendrite arm and subsequent formation of a cavity by the rejoining of the separated growth, (e) formation of a bent intermetallic and (f) growth of one intermetallic passing an obstructing intermetallic.

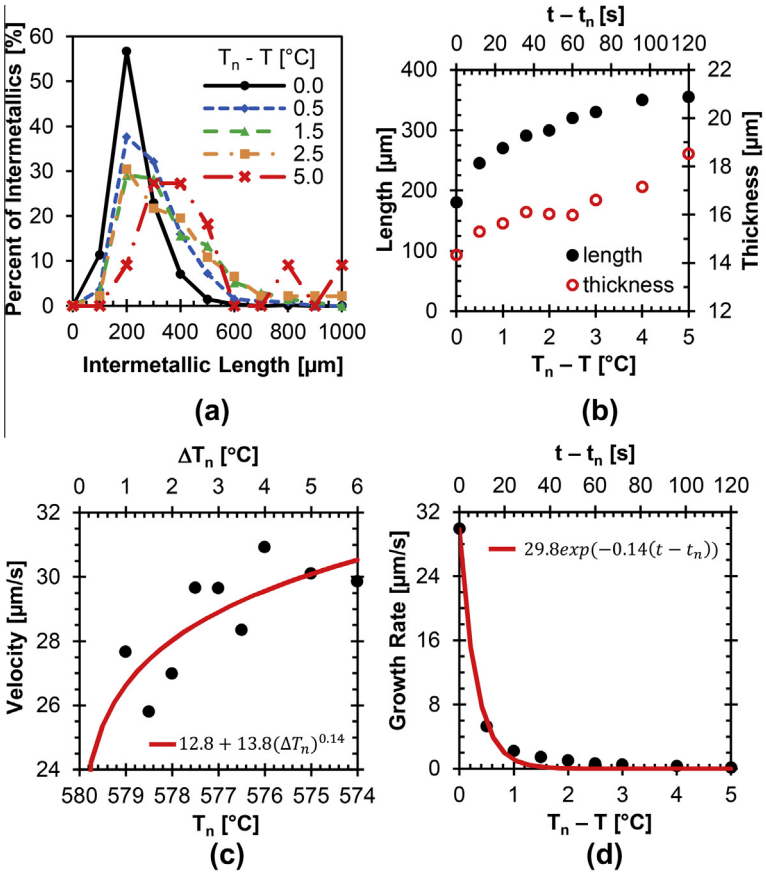

Fig. 10. β-Intermetallic growth characteristics: (a) distribution of intermetallic length, (b) average length and thickness of intermetallics as a function of temperature ($T_n - T$) and time ($t - t_n$) after nucleation, (c) average initial growth velocity as a function of nucleation temperature (T_n) and nucleation undercooling (ΔT_n), and (d) mean growth velocity as a function of temperature ($T_n - T$) and time ($t - t_n$) after nucleation.

arms, β-intermetallics continue to grow with ease in their preferred directions by wrapping around obstacles (arrow in Fig. 9d). Intermetallics are also observed to grow, or perhaps deform, into bent plates (Fig. 9e). Plates are also observed to grow around each other (Fig. 9f; the blue plate grows around the obstructing green plate).

To quantify the growth kinetics, which involves quantifying the evolution in plate length and thickness, the lengths in the directions given by both the first and third principal components of each β-intermetallic are measured, along with their changes in time (growth velocity). As each β-intermetallic nucleates at a different temperature, the distribution in maximum length for different undercooling relative to the nucleation temperature ($T_n - T$) is plotted in Fig. 10a. Just after nucleation, the distribution in β-intermetallic length is narrow; however, as time and undercooling increase, the distribution broadens because the plates themselves increase in size.

The initial intermetallic growth rate is unconstrained and thus very fast, as illustrated in Fig. 10b, where the average β-intermetallic length is 180 ± 5 μm immediately after nucleation. The average length of an intermetallic increases from 180 ± 5 to 300 ± 5 μm with a temperature increase of only 2 °C after nucleation, and in the subsequent 2 °C of cooling reaches 350 ± 5 μm. In contrast, the thickening rate of the plates, also shown in Fig. 10b, is found to be much slower than the lateral growth rate. This is most likely due to the slower attachment of atoms onto the facet plane [50]. Note that if the grain size and secondary arm spaces were smaller, then the growth of the intermetallics would be much more restricted. This could account for previous observations where the average β-intermetallic size was reduced when the α-Al grain size was refined via either faster cooling rates [51] or from the addition of grain refiners [52].

To investigate the mean initial growth velocity as a function of nucleation undercooling, the average initial growth velocity for the β-intermetallics nucleating at the same temperature (T_n) was calculated. Fig. 10c shows that the initial growth velocity of β-intermetallics increases with nucleation undercooling. The relationship between the initial β-intermetallic velocity and the nucleation undercooling can be described as a power function:

$$v = a + b(\Delta T_n)^m = 12.8 + 13.8(\Delta T_n)^{0.14} \quad (2)$$

where v is growth velocity and a, b and m are fitting parameters, calculated using nonlinear least-squares regression. This result confirms a strong contribution of undercooling with respect to the lateral growth of β-intermetallics.

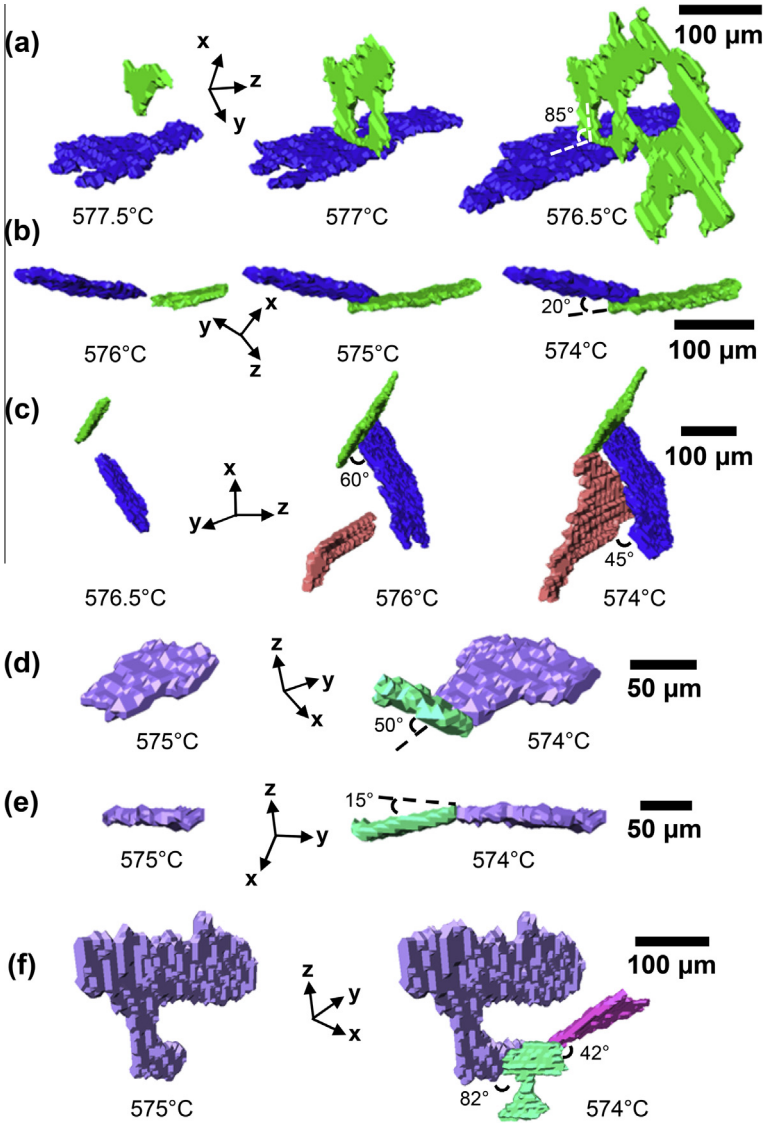

Fig. 11. Types of intermetallic-intermetallic interaction: (a–c) impingement mechanism and (d–f) potential branching mechanisms. Measurements of 3-D angles between each contact are also detailed.

The mean lateral growth velocity as a function of time (t) and temperature (T) after nucleation is illustrated in Fig. 10d for the cooling rate of 3 °C min^{-1}. It is worth noting that, unlike Fig. 10c, Fig. 10d shows the average growth velocity of β-intermetallics that share both the same temperature ($T_n - T$) and the same time ($t - t_n$) after nucleation. The mean growth velocity is observed to be highest at the first growth step (~30 μm s^{-1}). It then decreases exponentially with time, reaching ~1 μm s^{-1} 50 s after nucleation. A decrease in growth velocity with time can then be described as:

$$v = p \times \exp(q(t - t_n)) = 29.8 \times \exp(-0.14(t - t_n)) \quad (3)$$

where v is growth velocity, $t - t_n$ is the elapsed time after nucleation, and $p = 29.8$ and $q = -0.14$ are fitting parameters. Eq. (3) can also be formulated in terms of temperature, providing an easy-to-use equation for microstructural models predicting intermetallic growth.

These results compare well to prior studies in similar alloys, where a growth rate of 12.5 μm s^{-1} was measured (at a slower cooling rate of 1.4 °C min^{-1}) in the early stages of β-intermetallic growth [20], whilst a mean rate of 34 μm s^{-1} and a maximum of 100 μm s^{-1} were found at a much higher cooling rate (20 °C min^{-1}) [7]. After the initial rapid growth of the intermetallic, the growth rate decreases, as shown in Fig. 10d. This decrease is probably due to both solute depletion and the physical blocking caused by the surrounding aluminium dendrites.

3.4. Intermetallic–Intermetallic interactions

The intermetallics were frequently observed to interact with each other, as shown in Fig. 9f. Three types of interaction were classified in this study, as depicted in Fig. 11. The first type corresponds to an impingement mechanism. This occurs when two (or more) separated β-intermetallics

grow towards each other and impinge on one another. Impingement of β-intermetallics can occur at various angles: high (Fig. 11a), medium and low (Fig. 11b). Note that impingement does not stop intermetallic growth, as each β-intermetallic continues to grow both along the contact points and in other directions. Impingement of multiple β-intermetallics can also occur (Fig. 11c), leading to the formation of complex clusters of intermetallics.

The second type of interaction occurs when new β-intermetallics appear that are already in contact with pre-existing β-intermetallics, suggesting a branching mechanism, as previously observed in Ref. [20]. Similar to impingement, branching was observed at various angles: high, medium (Fig. 11d) and low (Fig. 11e). In a few cases, complex branching was observed (see Fig. 11f), where two separate β-intermetallics (green and pink) both appear to be branches of a single parent β-intermetallic (blue). However, it is important to note that events termed "branching" may be due to independently nucleating plates that grow sufficiently between scans to "impinge" on a pre-existing plate, and hence could be just poorly resolved impingement events. Experiments with increased temporal resolution would be necessary to fully understand and classify these interactions.

The third interaction is referred to as "unclassifiable" events, where two or more β-intermetallics appear together, already in contact, within a single scan. Improved temporal resolution is also required to further characterise this type of interaction.

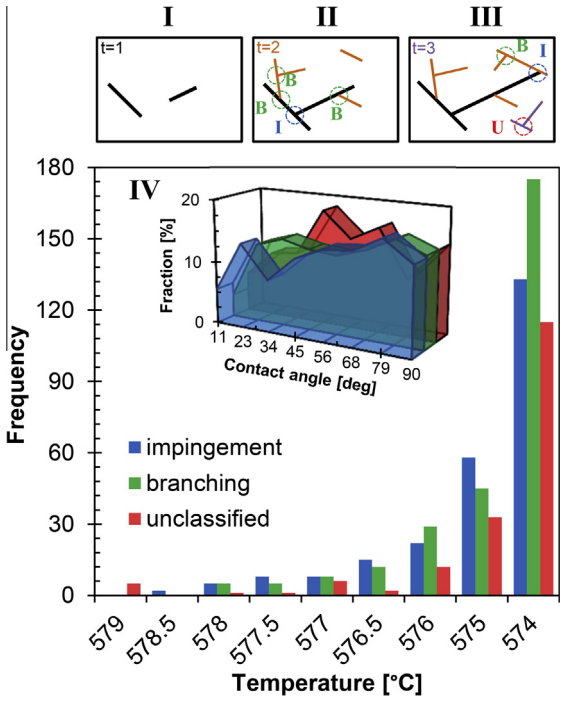

Fig. 12. The frequency of different types of intermetallic–intermetallic interaction with temperature. Insets I–III illustrate criteria used to classify growth interactions into (I) impingement, (B) branching and (U) unclassifiable. Inset IV plots the histogram of angles found between each contact over different types of interaction.

By classifying every intermetallic–intermetallic contact using the aforementioned criteria, the number of occurrences of different types of interaction as a function of temperature was obtained and is shown in Fig. 12. The three intermetallic–intermetallic interactions are schematically illustrated in insets I–III of Fig. 12. It is found that intermetallic–intermetallic contacts increase with decreasing temperature. All three types of interaction were observed at all temperatures, but branching and impingement are more commonplace (~40 and ~37%, respectively) than unclassifiable events. Further, angles between each intermetallic–intermetallic contact were measured in three dimensions for all three categories, and the results are plotted as a histogram in inset IV of Fig. 12. Each of the three types of interaction exhibits a large range of contact angles, with no clear preferential angle for any interaction type. This lack of a preferential contact angle further suggests that the branching mechanism (where a crystallographic angle [20] or twinning relationship [50,53] would be expected) may just be a poorly resolved impingement interaction.

4. Conclusions

The formation of β-Al_5FeSi intermetallics during solidification of an Al–7.5Si–3.5Cu–0.6Fe (wt.%) alloy was quantitatively investigated via 4-D synchrotron X-ray tomographic microscopy. Two in situ solidification experiments, under the same conditions, were performed at scan intervals of 72 and 12 s in order to observe both the slower kinetics of a full solidification sequence and the more rapid nucleation and initial growth of β-intermetallics, respectively.

The 12 s capture rate allowed, for the first time, the mechanisms of β-intermetallic nucleation and growth to be classified both qualitatively and quantitatively, with over 900 intermetallics measured. Four nucleation mechanisms were observed, with the most prevalent (~66%) being nucleation on/near the primary α-Al phase. The β-intermetallics were also found to have a strong preferential orientation parallel to the secondary dendrite arms of the α-Al dendrites, further supporting the hypothesis that they nucleate off the primary phase. The other ~34% of the intermetallics nucleated via oxides at the specimen and/or pore surfaces or via branching (i.e. self-nucleation). The relationship between nucleation density and undercooling was quantified using a Gaussian distribution, providing a convenient equation to be used in microstructural models.

In terms of intermetallic growth, several key observations were made. First, β-intermetallic plate growth was largely complete before the formation of the Al–Si eutectic. Second, intermetallics grew easily around obstacles, which included the primary phase and other intermetallics. Third, the main mechanism of large, interconnected, intermetallic cluster formation was determined to be impingement. Finally, an equation to describe intermetallic growth velocity was developed, with the mean lateral growth velocity

decreasing exponentially with time after an initial rapid growth spurt.

These insights into the nucleation mechanisms and growth dynamics of β-intermetallics are critical to the development of new alloys. They provide improved understanding of the mechanisms governing intermetallic formation and growth, which is critical for more accurate predictive models including β-intermetallics.

Acknowledgements

The authors acknowledge and thank the TOMCAT beamline, and particularly G. Mikuljan for his assistance with the setup. Thanks also to J. Wang and K. Kareh for help with commissioning of the in situ rig, material preparation and running of the experiments. The authors also thank the EPSRC (EP/I02249X/1), M-ORS, a Thai Government Scholarship, Ford Motor Company and the Research Complex at Harwell for financial, materials and facilities support. J.L.F. also acknowledges CCMX for funding.

References

[1] Kear BH, Giamei AF, Silcock JM, Ham RK. Scr Metall Mater 1968;2:287.
[2] Gladman T. P Roy Soc Lond A Mat 1966;294:298.
[3] Yi JZ, Gao YX, Lee PD, Lindley TC. Mater Sci Eng, A 2004;386:396.
[4] Puncreobutr C, Lee PD, Kareh KM, Connolley T, Fife JL, Phillion AB. Acta Mater 2014;68:42.
[5] Dash M, Makhlouf M. J Light Met 2001;1:251.
[6] Dinnis C, Taylor J, Dahle A. Metall Mater Trans A 2006;37:3283.
[7] Wang J, Lee PD, Hamilton RW, Li M, Allison J. Scripta Mater 2009;60:516.
[8] Belov NA, Aksenov AA, Eskin DG. Iron in aluminium alloys: impurity and alloying element (advances in metallic alloys). London: CRC Press; 2002.
[9] Shabestari SG. Mater Sci Eng, A 2004;383:289.
[10] Sha G, O'Reilly K, Cantor B, Worth J, Hamerton R. Mater Sci Eng, A 2001;304–306:612.
[11] Dinnis CM, Taylor JA, Dahle AK. Mater Sci Eng, A 2006;425:286.
[12] Roy N, Samuel A, Samuel F. Metall Mater Trans A 1996;27:415.
[13] Wang J, Li M, Allison J, Lee PD. J Appl Phys 2010;107:061804.
[14] Paray F, Kulunk B, Gruzleski JE. Int J Cast Met Res 2000;13:147.
[15] Lu L, Dahle A. Metall Mater Trans A 2005;36:819.
[16] Samuel AM, Samuel FH, Doty HW. J Mater Sci 1996;31:5529.
[17] Smith T, O'Reilly K, Kumar S, Stone I. Metall Mater Trans A 2013;44:4866.
[18] Allen CM, O'Reilly KAQ, Cantor B. Acta Mater 2001;49:1549.
[19] Kim B, Lee S, Lee S, Yasuda H. Mater Trans 2012;53:374.
[20] Terzi S, Taylor JA, Cho YH, Salvo L, Suéry M, Boller E, et al. Acta Mater 2010;58:5370.
[21] Yi J, Gao Y, Lee P, Flower H, Lindley T. Metall Mater Trans A 2003;34:1879.
[22] Sha G, O'Reilly KAQ, Cantor B, Titchmarsh JM, Hamerton RG. Acta Mater 2003;51:1883.
[23] Dinnis CM, Taylor JA, Dahle AK. Scripta Mater 2005;53:955.
[24] Fife JL, Rappaz M, Pistone M, Celcer T, Mikuljan G, Stampanoni M. J Synchrotron Radiat 2012;19:352.
[25] Stampanoni M, Groso A, Isenegger A, Mikuljan G, Chen Q, Bertrand A, et al. In: Proceedings of SPIE: developments in X-ray tomography V. p. 63180M.
[26] Mokso R, Marone F, Stampanoni M. AIP Conf Proc 2010;1234:87.
[27] Marone F, Munch B, Stampanoni M. In: Proceedings of developments in X-ray tomography VII. p. 780410.
[28] Marone F, Stampanoni M. J Synchrotron Radiat 2012;19:1029.
[29] Studholme C. Pattern Recogn 1999;32:71.
[30] Weickert J, Haar B, Viergever R. IEEE Trans Image Process 1998;7:398.
[31] Adams R, Bischof L. IEEE Trans Pattern Anal 1994;16:641.
[32] Crocker JC, Grier DG. J Colloid Interface Sci 1996;179:298.
[33] Puncreobutr C, Lee P, Hamilton R, Phillion A. JOM 2012;64:89.
[34] Yue S, Lee PD, Poologasundarampillai G, Jones JR. Acta Biomater 2011;7:2637.
[35] Dinnis CM, Dahle AK, Taylor JA. Mater Sci Eng, A 2005;392:440.
[36] Mathiesen R, Arnberg L, Li Y, Meier V, Schaffer P, Snigireva I, et al. Metall Mater Trans A 2011;42:170.
[37] Du Y, Schuster JC, Liu Z-K, Hu R, Nash P, Sun W, et al. Intermetallics 2008;16:554.
[38] Lee PD, Hunt JD. Scripta Mater 1997;36:399.
[39] Veldman NM, Dahle A, StJohn D, Arnberg L. Metall Mater Trans A 2001;32:147.
[40] Oldfield W. Trans Am Soc Met 1966;59:945.
[41] Gandin CA, Rappaz M. Acta Metall Mater 1994;42:2233.
[42] Narayanan L, Samuel F, Gruzleski J. Metall Mater Trans A 1994;25:1761.
[43] Miller DN, Lu L, Dahle AK. Metall Mater Trans B 2006;37:873.
[44] Sigworth G, Campbell J. Int J Metalcast 2009;3:65.
[45] Narayanan LA, Samuel FH, Gruzleski JE. Metall Mater Trans A 1995;26:2161.
[46] Cao X, Campbell J. Metall Mater Trans A 2003;34:1409.
[47] Cho YH, Lee HC, Oh KH, Dahle AK. Metall Mater Trans A 2008;39:2435.
[48] Phillion AB, Lee PD, Maire E, Cockcroft SL. Metall Mater Trans A 2008;39:2459.
[49] Oda M. Soils Found 1982;22:97.
[50] Sha G, O'Reilly K, Cantor B. Mater Sci Forum 2006;519–521:1721.
[51] Liu L, Mohamed AMA, Samuel AM, Samuel FH, Doty HW, Valtierra S. Metall Mater Trans A 2009;40:2457.
[52] Khalifa W, Samuel F, Gm Nserc U, Gruzleski J, Doty H, Valtierra S. Metall Mater Trans A 2005;36:1017.
[53] Hansen V, Hauback B, Sundberg M, Romming C, Gjonnes J. Acta Crystallogr B 1998;54:351.